



Cite this: *Phys. Chem. Chem. Phys.*,
2022, 24, 9432

First-principles calculations of bulk, surface and interfacial phases and properties of silicon graphite composites as anode materials for lithium ion batteries†

Stéphane B. Olou'ou Guifo,^{ab} Jonathan E. Mueller,^{id}*^a David Henriques^b and Torsten Markus^b

The high energy density offered by silicon along with its mineralogical abundance in the earth's crust, make silicon a very promising material for lithium-ion-battery anodes. Despite these potential advantages, graphitic carbon is still the state of the art due to its high conductivity and structural stability upon electrochemical cycling. Composite materials combine the advantages of silicon and graphitic carbon, making them promising materials for the next generation of anodes. However, successfully implementing them in electric vehicles and electronic devices depends on an understanding of the phase, surface and interface properties related to their performance and lifetime. To this end we employ electronic structure calculations to investigate crystalline silicon-graphite surfaces and grain boundaries exhibiting various orientations and degrees of lithiation. We observe a linear relationship between the mixing enthalpies and volumes of both Li–Si and Li–C systems, which results in an empirical relationship between the voltage and the volume expansion of both anode materials. Assuming thermodynamic equilibrium, we find that the lithiation of graphite only commences after Li_xSi has been lithiated to $x = 2.5$. Furthermore, we find that lithium ions stabilize silicon surfaces, but are unlikely to adsorb on graphite surfaces. Finally, lithium ions stabilize silicon-graphite interfaces, increasing the likelihood of adhesion as core@shell over yolk@shell configurations with increasing degree of lithiation. These observations explain how lithium might accelerate the crystallization of silicon–graphite composites and the formation of smaller nanoparticles with improved performance.

Received 26th November 2021,
Accepted 31st March 2022

DOI: 10.1039/d1cp05414g

rsc.li/pccp

Introduction

Silicon (Si) is one of the most attractive anode materials for the next generation of lithium (Li)-ion batteries due to its high gravimetric and volumetric capacities in combination with its low voltage. However, silicon-based anodes undergo substantial volumetric expansion and contraction during repeated lithiation and delithiation cycles, which result in crack formation and excessive solid electrolyte interphase (SEI) growth. The resulting particle degradation and pulverization can damage the polymer binder, leading to a loss of electrical contact and poor ionic conductivity between the anode particles.^{1–10} As a result, the utilization of pristine silicon as an anode material leads to shortened battery lifetimes and safety concerns. By com-

binning silicon with graphitic carbon (C), which offers higher electrical conductivity, electrochemical-cycling stability and mechanical durability than silicon,¹¹ composite materials can be formed, which are capable of maintaining high capacities for a large number of charge–discharge cycles.^{12–15} Further improvements can be realized by forming selecting composites with a suitable micro- or nanostructure,^{8,14–24} which utilizes well-placed surfaces and grain boundaries to absorb a substantial amount of the mechanical loading and thereby reduce the risk of crack formation and pulverization. Furthermore, the appearance of inhomogeneities in the state of charge (SoC) across the electrode can be minimized by providing suitable channels for lithium ion transport along interfaces. Indeed, a system made up of nanoparticles is generally less sensitive to chemomechanical inhomogeneities, because of the high concentration of surfaces and grain boundaries. Therefore, a fundamental understanding of the properties and performance of nanostructured Si–C anodes depends on a detailed knowledge of their interfaces.

A first step toward understanding the aging of silicon–carbon-based anodes is to identify the phases formed during

^a Volkswagen Group, Berliner Ring 2, D-38436, Wolfsburg, Germany.

E-mail: jonathan.edward.mueller@volkswagen.de

^b Institute of Materials Science and Engineering, Mannheim University of Applied Sciences, Paul-Wittsack-Straße 10, D-68153, Mannheim, Germany

† Electronic supplementary information (ESI) available. See <https://doi.org/10.1039/d1cp05414g>

electrochemical cycling. Along these lines, several research groups have studied (de)lithiation processes and equilibrium states of Li–Si^{25–29} and Li–C^{30–35} systems. Although crystalline lithium silicide (c-Li_xSi) phases are more stable than amorphous lithium silicide (a-Li_xSi) phases with the same composition,²⁵ the amorphous phases are frequently observed in these studies because electrochemical cycling leaves insufficient time for the system to reach equilibration. Besides the stabilities of various bulk phases, a fundamental description of the aging of silicon-carbon-based anodes rests on the thermodynamics of the reacting interfaces during electrochemical cycling. Indeed, unless intra- and interparticle interfaces remain stable as they facilitate the transport of lithium ions during cycling, low Coulombic efficiencies and shortened lifetimes will result. Very few studies treat surface and grain boundary properties of lithiated silicon (Li_xSi or Li_xSi_{1-x}) or graphite phases (Li_yC or Li_yC_{1-y}). Nonetheless, initial insights can be obtained by considering the unary systems as did Tran *et al.*, who reported elemental surface tensions of 1.30...2.13 J m⁻² and 0.46...0.54 J m⁻² depending on the surface orientations and reconstructions of silicon and lithium.³⁶ Using experimental measurements and DFT calculations, Hara *et al.* found that the surface tension of a-Si lies below that of c-Si³⁷ and attributed their finding to the weaker bonds in a-Si resulting in a lower mass density. Using first-principles simulations, Chia-Yun *et al.* found that the surface tension of a-Li_xSi phases decreases with increasing lithiation.³⁸ They attributed this to the weakness of Li–Si and Li–Li bonds compared to Si–Si bonds. Thus, pristine silicon can be considered as the upper bound and lithium as the lower bound for the surface tensions of Li_xSi phases.

Ooi *et al.* investigated the structural properties and the surface stability of graphite computationally. They reported surface tensions of the same order of magnitude as those obtained experimentally, although the weak van der Waals interactions between the graphite layers were not accurately depicted in their theoretical model.³⁹

Due to the complexity of Si–C composite anodes, *in-situ* investigations of grain boundary and surface energies in Si–C composite anodes have not yet been carried out. However, while failing to provide direct evidence of atomistic details, electrochemical measurements can be used in conjunction with atomistic modeling to shed light on underlying atomistic structures and processes. In this regard, Zhang *et al.* achieved higher cycling stability by coating silicon with graphite and modeled their findings using atomistic simulations of a silicon slab and one or two graphene layers.⁴⁰ Feng *et al.* demonstrated that the irreversible capacity of silicon-graphite systems can be attributed to the shorter lengths of Li–Si and Li–C bonds at the interfaces, by inserting lithium into empty sites within the silicon-graphene composite and performing *ab initio* molecular dynamics (AIMD) simulations.⁴¹ Using the same atomistic model, they determined that a graphene coating results in a slight volume decrease which reduces mechanical failure and leads to a higher voltage.

The aim of this paper is to provide new theoretical insights into the influence of the micro- or nanostructure on the stability of Si–C composite anodes by using atomistic simulations to study

the bulk and interfacial properties of representative models. First, we discuss the thermodynamic properties of variously lithiated Li_xSi and Li_yC bulk phases. Second, we investigate the surface formation of stable Li_xSi or Li_yC bulk phases, considering various surface orientations for each phase. Third, we combine the surface structures of different phases to form interfacial Li_xSi–Li_yC (*i.e.* solid–solid) systems. Fourth, we compare the chemical stability of these solid interfaces with the stability of Li_xSi–void–Li_yC (*i.e.* solid–void–solid) interfaces, which we treat as pairs of surfaces separated by a vacuum gap. Finally, we conclude by analyzing the charge densities of the surface and interface structures to obtain further insights into their relative stabilities.

Methodology

Ab initio calculations, based on the principles of quantum mechanics, are routinely used to determine the electronic ground states of materials at absolute zero in a vacuum (*i.e.* $T = 0$ K, $p = 0$ atm). For many solid-state materials temperature and pressure effects under standard conditions (*i.e.* $T = 298$ K, $p = 1$ atm) are small enough to ignore. It is within the framework of these assumptions that we apply *ab initio* calculations to study the atomistic structure–property relationships of Si–C composite materials.

Theoretical approach

The thermodynamic stability of heterogeneous (*i.e.* multiphase) Si–C systems at various degrees of lithiation is related to their Gibbs free energies, ΔG , which are functions of temperature and pressure.^{42,43} Our *ab initio* simulations provide energies for the materials at zero temperature and pressure, *i.e.* 0 K and 0 atm, and do not include zero-point corrections. For the structures considered in this work, the mechanical contribution to the free energy (*i.e.* $P\Delta V$) is ~ 0.01 meV at atmospheric pressure, and the entropic term (*i.e.* $T\Delta S$) is ~ 25 meV at room temperature (RT).^{44–48} Provided that differences in the Gibbs free energy, ΔG , which describes isothermal–isobaric equilibrium, are significantly larger than these mechanical and thermal contributions, then the DFT total energy, E , is a reasonable approximation for the Gibbs energy:

$$\Delta G = \Delta E - T\Delta S + P\Delta V \cong \Delta E. \quad (1)$$

By treating each single phase, *i.e.* Li_xSi_{1-x} and Li_yC_{1-y}, in the lithiated Si–C two-phase anode separately, phase diagrams can be constructed on the basis of the Gibbs free energies of the pure standard-state (*i.e.*, crystalline) components and the Gibbs free energy for a mixture, which is defined as

$$\Delta G_{\text{f}}(X^{\phi}) = G_{\text{Li}_x\phi[\text{H}]_{1-x\phi}} - X^{\phi}\mu_{\text{Li}}^0 - (1 - X^{\phi})\mu_{[\text{H}]}^0. \quad (2)$$

Here [H] refers to the host electrode material (*i.e.* silicon or carbon) and X^{ϕ} denotes the lithium content in a phase ϕ . Similarly, the mixing or formation volume is expressed as

$$\Delta V_{\text{f}}(X^{\phi}) = V_{\text{Li}_x\phi[\text{H}]_{1-x\phi}} - X^{\phi}V_{\text{Li}}^0 - (1 - X^{\phi})V_{[\text{H}]}^0.$$

Assuming the homogeneity of the system, the chemical potential of lithium ions is defined as

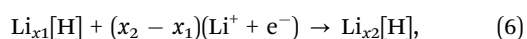
$$\mu(X) = \left. \frac{\partial G_{\text{Li}_x\phi[\text{H}]_{1-x\phi}}}{\partial X_{\text{Li}}^\phi} \right|_{X_{[\text{H}]}} \quad (4)$$

$$\text{or } \mu(x) = \frac{\partial G_{\text{Li}_x[\text{H}]}}{\partial x}$$

Hence, the voltage with respect to metallic lithium, with chemical potential μ_0 , can be expressed at any lithium content x as

$$U(x) = -\frac{1}{z_{\text{Li}}\mathcal{F}}(\mu(x) - \mu_0). \quad (5)$$

If the stable structures are known from the binary phase diagram, the equilibrium voltage can be calculated more accurately from the two-phase reaction from reactant to product:^{46,49–51}



$$U(x_1, x_2) = -\frac{G_{\text{Li}_{x_2}[\text{H}]} - G_{\text{Li}_{x_1}[\text{H}]} - (x_2 - x_1)\mu_0}{z_{\text{Li}}\mathcal{F}(x_2 - x_1)}, \quad (7)$$

where $z_{\text{Li}} = 1$ denotes the number of elementary charges of each lithium cation and \mathcal{F} is the Faraday constant. The theoretical capacity of the electrode, $\text{Li}_x[\text{H}]$, is formulated with respect to the electrode mass as

$$Q_{\text{th},m} = \frac{n_e\mathcal{F}}{M_{\text{Li}_x[\text{H}]}} \quad (8)$$

and with respect to the electrode volume as

$$Q_{\text{th},V} = \frac{n_e\mathcal{F}}{V_{\text{Li}_x[\text{H}]}} \quad (9)$$

at any lithium content x (*i.e.* $x = x_{\text{max}}$ for the lithiated state and $x = 0$ for the delithiated state), where n_e is the maximum number of transferable electrons per mole of the host material [H].

Surfaces (*i.e.* solid–vacuum interfaces) are modelled using a two-dimensionally periodic film or slab surrounded by vacuum. The surface tension of a phase ϕ with surface orientation ω is determined as the partial derivative of the Gibbs energy with respect to the surface area A_ω^ϕ and is computed as^{36,52}

$$\gamma_\omega^\phi = \frac{1}{2A_\omega^\phi}(E_\omega^\phi - E^\phi), \quad (10)$$

where E_ω^ϕ is the DFT energy of a slab with surface orientation ω , and E^ϕ is the DFT energy of the same number of atoms in the bulk phase. Solid–void–solid interfaces are not modeled directly but instead are treated as combinations of two parallel, non-interacting surfaces separated by vacuum, whose interface tension is determined as

$$\gamma_{\omega_1\omega_2}^{\phi_1/\phi_2} = \gamma_{\omega_1}^{\phi_1} + \gamma_{\omega_2}^{\phi_2}. \quad (11)$$

A solid–solid interface between two phases ϕ_1 and ϕ_2 , with the respective surface orientations ω_1 and ω_2 , has an interfacial

tension that can be expressed as^{52,53}

$$\gamma_{\omega_1\omega_2}^{\phi_1/\phi_2} = \frac{1}{2A_{\omega_1\omega_2}^{\phi_1/\phi_2}}(E_{\omega_1\omega_2}^{\phi_1/\phi_2} - E^{\phi_1} - E^{\phi_2}), \quad (12)$$

where $E_{\omega_1\omega_2}^{\phi_1/\phi_2}$ is the energy of the two-phase system containing both interfaces. E^{ϕ_1} and E^{ϕ_2} are the energies of the isolated bulk phases. In order to quantify the adhesion between the two surfaces, the work of adhesion per area unit can be defined as

$$\gamma_W = \gamma_{\omega_1\omega_2}^{\phi_1/\phi_2} - \gamma_{\omega_1\omega_2}^{\phi_1/\text{void}/\phi_2}. \quad (13)$$

A negative work of adhesion suggests that adhesion is spontaneous (*i.e.* exothermic), whereas a positive work means that compressive energy is required to bring the surface into contact with each other.

The volume strain arising at an interface can be expressed as:

$$\varepsilon_V \omega_1\omega_2^{\phi_1/\phi_2} = \frac{V_{\omega_1\omega_2}^{\phi_1/\phi_2} - V_{\phi_1} - V_{\phi_2}}{V_{\phi_1} + V_{\phi_2}} \quad (14)$$

Additionally, each slab surface is strained parallel to the interface, with a strain given by:

$$\begin{aligned} \varepsilon_1 \omega_1\omega_2^{\phi_1/\phi_2} &= \frac{A_{\omega_1\omega_2}^{\phi_1/\phi_2} - A_{\omega_1}^{\phi_1}}{A_{\omega_1}^{\phi_1}}, \quad \varepsilon_2 \omega_1\omega_2^{\phi_1/\phi_2} \\ &= \frac{A_{\omega_1\omega_2}^{\phi_1/\phi_2} - A_{\omega_2}^{\phi_2}}{A_{\omega_2}^{\phi_2}}. \end{aligned} \quad (15)$$

The Gibbs phase rule⁴² defining the minimal number of degrees freedom f in a system with N_i components, N_ϕ phases and N_j independent defects at isothermal–isobaric conditions is

$$f = N_i - N_\phi + N_j, \quad (16)$$

and can be applied to lithiated, two-phase Si–C anodes. Each binary subsystem consisting of a homogeneously lithiated anode host material, [H] (*e.g.* silicon, carbon), contributes to a degree of freedom, $f = 1$, reflecting the variable lithium content, X , in $\text{Li}_x[\text{H}]_{1-x}$. The presence of surfaces increases the number of degrees of freedom to $f = 2$ due to the additional energy contributions. The equilibrium at the interfaces between Li_xSi and Li_yC phases is governed by the total lithium mole ratio, $X + Y$, in $\text{Li}_x\text{Si}_{1-x}\text{Li}_y\text{C}_{1-y}$, and by the interfacial properties. Here, the lithium contents, X in silicon and Y in carbon, are related to each other by the common lithium chemical potential shared by both subsystems.

Computational model

Electronic structure calculations were carried out in the context of density functional theory (DFT), which was originally formulated by Hohenberg and Kohn (HK)⁵⁴ and developed further by Kohn and Sham (KS).⁵⁵ Periodic simulations were performed using the Vienna *Ab initio* Simulation Package (VASP),⁵⁶ which is based on the projector augmented wave (PAW) method.^{57,58} Exchange–correlation effects were described using the optB86b method, which corrects the generalized gradient approximation developed by Perdew, Burke and Ernzerhof (GGA-PBE)⁵⁹ with the

Becke 86 exchange functional.^{60,61} This correction is essential for accurately describing weak van der Waals (vdW) interactions between the graphite layers.^{34,62} For several simulations of graphitic surfaces a semi-empirical force field correction for van der Waals interactions is added to the GGA-PBE method using the DFT-D2 ansatz developed by Grimme.⁶³ The electronic ground state of a given set of nuclear coordinates is determined by solving the KS equations iteratively, and the nuclear coordinates are optimized by equilibrating the Hellmann–Feynman (HF) forces.⁶⁴ Geometry optimization is carried out using the conjugate gradient (CG) approach and the residual minimization scheme known as the direct inversion in the iterative subspace (RMM-DIIS) method. The self-consistent-field (SCF) calculations of the KS equations are carried out with a cutoff energy of 520 eV for the plane waves, an energy convergence of 10^{-6} eV and a k -spacing in the Brillouin zone of 0.15 \AA^{-1} described by the Monkhorst–pack method with a Gamma-center k -grid.⁶⁵ Gaussian smearing is used as the integration scheme for determining the partial occupancy of each orbital with a smearing width of 0.05 eV while the tetrahedron method with Blöch corrections is used to determine the electronic density of states and the charge densities. The non-local exchange is described by the Blocked Davidson iteration scheme. The HF-forces on the atomic nuclei are equilibrated with a convergence of 0.01 eV \AA^{-1} . Initially we optimized the spin polarization of the structures; however, after verifying that none of the structures calculated early on were spin polarized (as one would have intuitively expected); the computational expense of later calculations was reduced by performing calculations without spin polarization. High-throughput (HT) algorithms are used to simultaneously compute the various bulk, slab and two-phase systems and automatically output the results for analysis.

The starting structuring for most of the $\text{Li}_x\text{Si}_{1-x}$ and $\text{Li}_y\text{C}_{1-y}$ phases studied throughout this work were taken from the Materials Project database.⁶⁶ Additional binary $\text{Li}_x\text{Si}_{1-x}$ phases investigated by Valencia-Jaime *et al.*²⁸ were also taken into account. The additional intermediate structures in the Li–C system were obtained using the UNCLE method mentioned in Section 2.2). The correction of van der Waals bonds using the optB86b method reveals that hexagonal graphite with the space group $P6_3/mmc$ is slightly more stable than orthorhombic graphite with the space group $Cmme$ (formerly $Cmma$) in contrast to the results using GGA-PBE exchange–correlation functionals. The energy difference between both structures is around $0.193 \text{ kJ mol}^{-1}$ per carbon atom whereas the GGA-PBE method predicts that each carbon atom of the $Cmme$ space group is rather energetically more stable by $0.003 \text{ kJ mol}^{-1}$. Furthermore, after applying the van der Waals interaction correction, hexagonal graphite exhibits a higher mass density of 2.294 g cm^{-3} due to the decrease in the interlayer distance to 3.298 \AA compared with orthorhombic graphite, which has a mass density of 2.266 g cm^{-3} and an interlayer distance of 3.339 \AA . Nevertheless, both carbon allotropes exhibit AB-stacking, and only differ in the horizontal placement of the A and B graphene layers. Based on experimental observations, hexagonal graphite with the space group is indeed the most common allotrope of pristine carbon minerals at standard

temperature and pressure (STP).⁶⁷ Therefore, hexagonal graphite is taken as a reference for computing the phase diagram of carbonaceous structures. In contrast to the two-dimensional graphite structure, the Li–Si system is barely affected by the van der Waals corrections of the GGA-PBE functionals since covalent and ionic bonding predominate the interatomic interactions in all spatial directions. Body-centered cubic (bcc) lithium metal ($Im\bar{3}m$ space group) and c-Si with a cubic diamond structure ($Fd\bar{3}m$ space group), which are the most stable elemental crystals, are used as stability references for the $\text{Li}_x\text{Si}_{1-x}$ phases. These reference structures are shown in Fig. 2.

The UNiversal CLuster Expansion (UNCLE)⁶⁸ was utilized in conjunction with VASP to generate representative structures of lithiated graphite phases with varying degrees of lithiation. A maximal supercell size of 10 LiC_6 unit cells was allowed in generating these representative Li_yC_6 structures ($0 \leq y \leq 1$).

To aid in the relaxation of cells with surfaces and interfaces, *ab initio* molecular dynamics (AIMD) simulations were performed within the NVE ensemble. The temperature was initialized at 500 K and molecular dynamics were performed for 400 fs using a time step of 2 fs, before performing a geometry minimization on the structure with the lowest energy. Slab geometries include a vacuum region of at least 13 \AA , so that interactions between periodic images of the slab's surfaces are negligible. The cell parameters used in slab models are based on the optimized cell parameters for the related bulk structure and are fixed during structure relaxation along with atoms near the center of the slab (25%...50% of all atoms), which mimic the response of bulk atoms during surface relaxation. For models of solid interfaces or grain boundaries, a full geometry optimization including all atomic coordinates and simulation cell parameters is carried out in order to find the equilibrium interface thickness as well as the optimal twist and tilt angles. Each solid interface model is initialized using the Interface Builder tool in MedeA,⁶⁹ which identifies symmetric correlations between the two adjacent slabs and then combines strained slabs to create a periodic system containing two interfaces. The strain applied to each slab is determined by comparing the stiffness and thickness of each slab. A mismatch tolerance of 10% for the initial area, lengths and angles is allowed in the automated creation of potential interfacial surfaces with no more than 200 atoms. The system exhibiting the lowest total length and angle mismatch is chosen as the representative model. To create the interfacial model an initial gap of 3 \AA is added to the cell length perpendicular to the interfaces since the true interfacial gap is not known prior to performing energy minimization.

Results and discussion

Thermodynamic phase stability and electrochemical behavior

The formation energies and molar volumes we calculated using DFT for Li–Si and Li–C binary systems are reported as binary phase diagrams in Fig. 1. Experimental data reported by Valencia-Jaime *et al.*²⁸ and Sangster⁷⁰ are plotted for comparison.

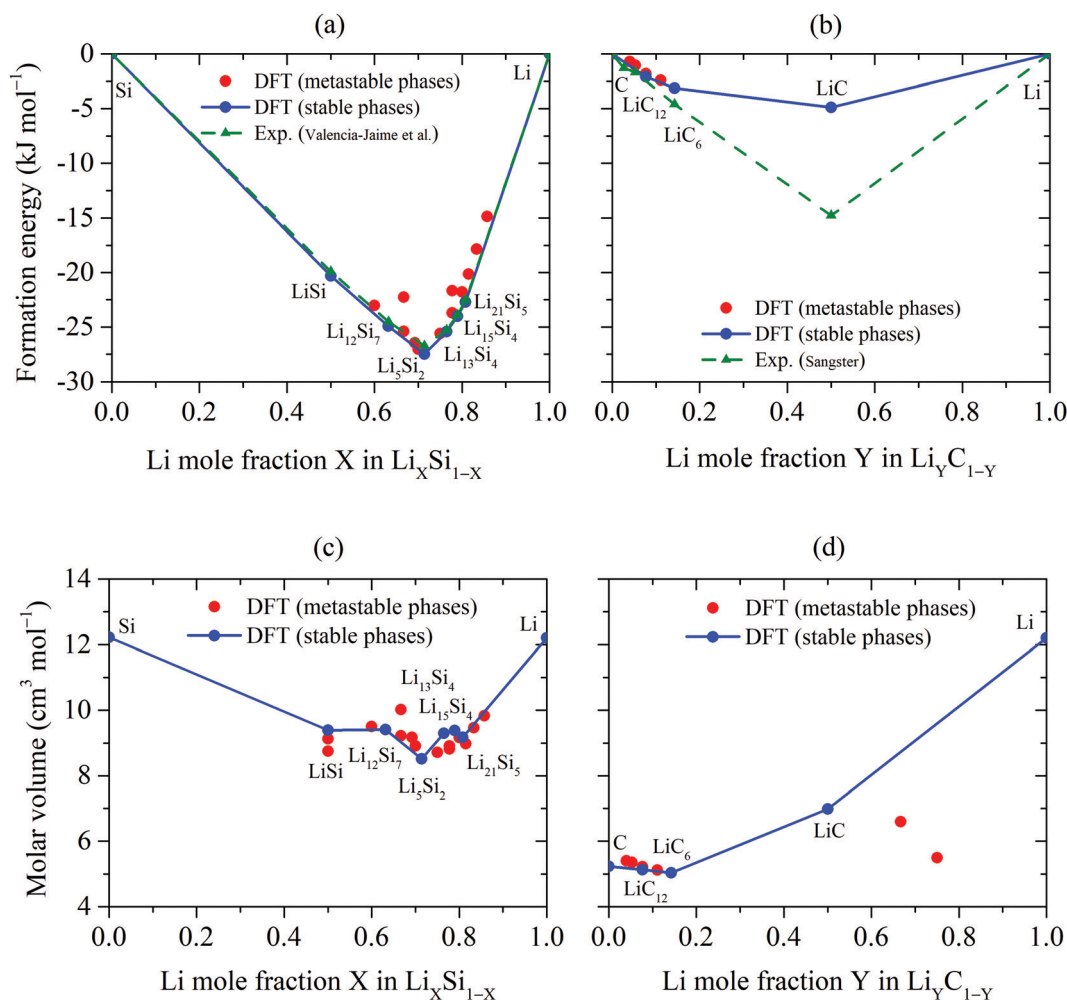


Fig. 1 Ground state phase properties of binary Li–Si and Li–C systems. Calculated ground state phase diagrams for (a) Li–Si and (b) Li–C, including stable (blue dots) and metastable (red dots) phases, are plotted alongside the experimental heats of formation reported by Valencia-Jaime *et al.*²⁸ and Sangster⁷⁰ (green dashed lines with triangles). The molar volumes are plotted in (c) and (d) for the Li_xSi and Li_yC phases, respectively. The compositions of stable phases (blue dots) are listed in the diagram. A blue ground state line connects the stable states.

As can be observed in Fig. 1(a), the six stable binary Si–Li phases we identified correspond with experimentally known stable phases and their formation energies. Our phase diagram is also in agreement with previous atomistic simulations^{25,28} as well as with experimental data,^{28,70–75} particularly in the cases of the tetragonal LiSi phase ($I4_1/a$ phase group) (see Fig. 2) and the trigonal Li_5Si_2 phase ($R\bar{3}m$ space group). However, our simulations fail to predict the cubic $\text{Li}_{22}\text{Si}_5$ phase ($F\bar{4}3m$ space group), which is found to be stable experimentally, and instead predict that it lies 1.7 kJ mol⁻¹ above the convex energy hull. This discrepancy might be due to temperature effects that our calculations don't account for. Alloying silicon and lithium results in volume changes as shown in Fig. 1(c). For the stable phases, the molar volume tends to be proportional to formation energy. Hence, Li_5Si_2 exhibits the lowest formation energy and the smallest molar volume. This trend can be explained by the shift from predominantly ionic bonding at $x = 2.5$ in Li_xSi to the detriment of covalent or metallic bonding exhibited by the unary crystals. Phases with a lithium content $x < 1$, such as

the LiSi_3 phases with the space groups $P6_3/mmc$ and $I4/mmm$, are unstable, exhibiting formation energies of 17.3 kJ mol⁻¹ and 18.0 kJ mol⁻¹, respectively. These also include lithium interstitials in silicon, which our DFT calculations predict to be unstable, with a formation energy of 29.4 kJ mol⁻¹. Indeed, the frequently observed two-phase lithiation of silicon anodes^{76,77} suggests that a minimum Li concentration (*i.e.* $x = 1$ in crystalline Li_xSi) is required to break covalent Si–Si bonds and replace them with Li–Si ionic bonds. This two-phase lithiation precedes by means of a phase change mechanism occurring at particles' surfaces and grain boundaries. An exothermically dissolved dopant in silicon can accelerate the lithiation process by reducing the formation energy of lithium interstitials. In fact, by facilitating the mixing of lithium and silicon within the bulk structure the rate limiting interfacial phase change constraints would be relaxed due to the faster lithium ion flux.

In contrast to silicon, the two-dimensionality of the graphite structure allows lithium ions to intercalate with relatively low energy variations up to a concentration of one lithium atom per

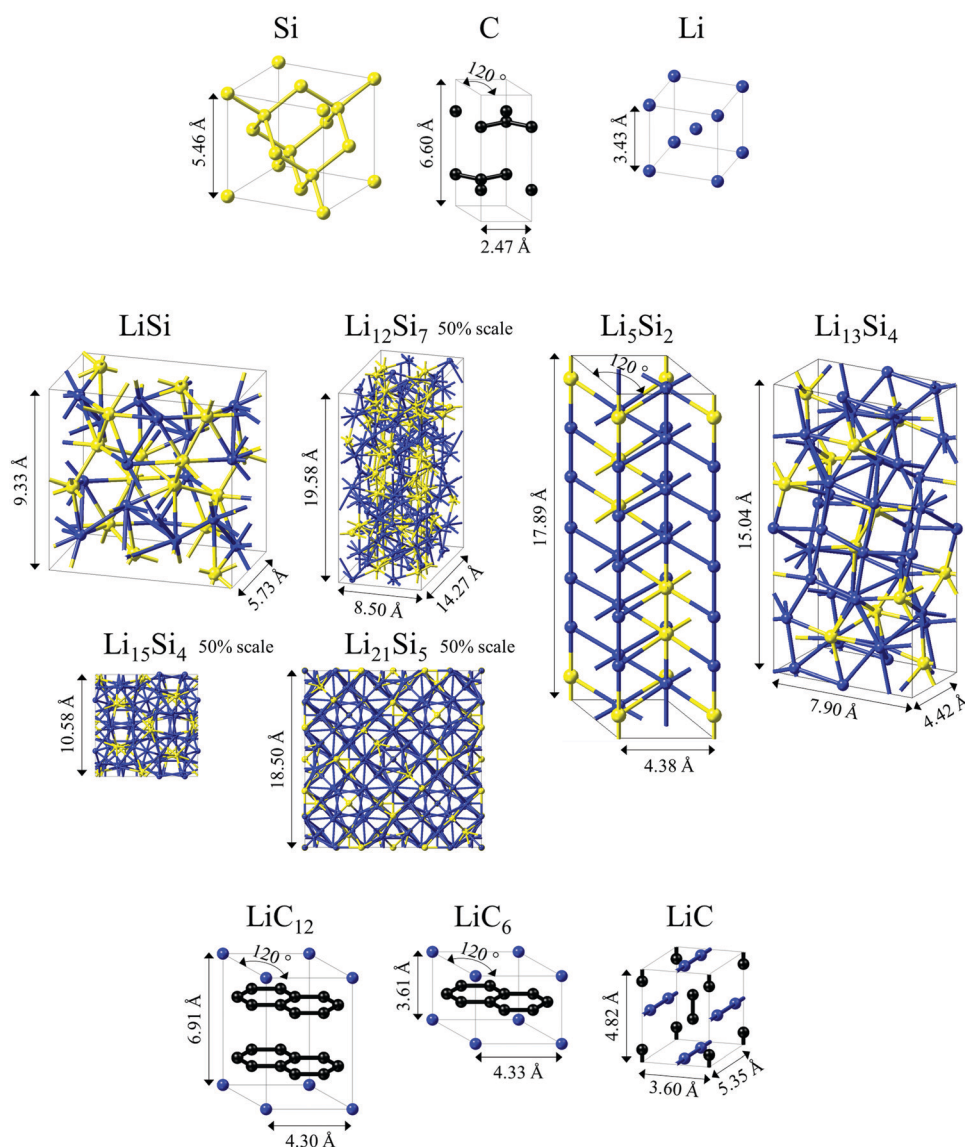


Fig. 2 Crystal structures of binary Li–Si and Li–C phases. Lithium, silicon and carbon atoms are blue, yellow and black, respectively. The elemental unit cells of silicon (cubic, $Fd\bar{3}m$), carbon (hexagonal, $P6_3/mmc$) and lithium (cubic, $Im\bar{3}m$) are used as reference states for calculating the mixing energy and volume. For the Li–Si system, the binary phases lying on the ground state line are LiSi (tetragonal, $I4_1/a$), $Li_{12}Si_7$ (orthorhombic, $Pnma$), Li_5Si_2 (trigonal, $R\bar{3}m$), $Li_{13}Si_4$ (orthorhombic, $Pbam$), $Li_{15}Si_4$ (cubic, $I\bar{4}3d$) and $Li_{21}Si_5$ (cubic, $F\bar{4}3m$). The stable phases of the Li–C system are LiC_{12} (hexagonal, $P6/mmm$), LiC_6 (hexagonal, $P6/mmm$) and LiC (cubic, $Immm$). Fictive bonds are added between neighboring atoms within 1.2 Å of each other.

hexagonal C_6 cluster. As a result, the lithiation of graphite up to that point only results in small volume changes (see Fig. 1(d)). Our UNCLE simulations provided numerous intermediate structures between C_6 and LiC_6 (e.g. LiC_{60} , LiC_{48}). In order to minimize the cost-benefit ratio of our simulations we only considered structures containing less than 200 atoms. As shown in Fig. 1(b) the formation energies we predict for the graphitic phases are in good agreement with experimental results. Beyond the graphitic region a stable Li_yC phase exists at $y = 1$. Hence, at thermodynamic equilibrium lithium plating doesn't occur immediately following the overlithiation of LiC_6 but rather following the formation of this orthorhombic phase with $Immm$ space group, which is often written as

Li_2C_2 due to the presence of carbon dimers.⁷⁸ Based on the thermomechanical measurements reported by Sangster *et al.*⁷⁰ this phase is significantly more exothermic than our simulations predict. Lin *et al.*⁷⁸ demonstrated the difficulty of accurately describing both graphitic and non-graphitic systems with a single DFT-based approach. Thus, by employing DFT-D2 we are able to obtain a more accurate formation energy of $-12.6 \text{ kJ mol}^{-1}$ (vs. the experimental value of $-14.8 \text{ kJ mol}^{-1}$); however, this approach results in less accurate formation energies for graphitic (Li_yC_6 with $0 \leq y \leq 1$) compounds as well as for the Li_xSi phases. Thus, we consider the optB86b method to be the best compromise for studying the Li–Si–C system.

At thermodynamic equilibrium, the volume expansion of the anode host materials can be determined from the molar volumes of the stable phases shown in Fig. 1(c and d). Due to the lower formation energy of $\text{Li}_x\text{Si}_{1-x}$ phases, silicon anodes are more susceptible to problems associated with aging such as thermal runaway than graphite anodes are. Furthermore, a correlation between the formation energies and the mixing volumes of both $\text{Li}_x\text{Si}_{1-x}$ and $\text{Li}_y\text{C}_{1-y}$ phases can be observed in Fig. S1 (ESI[†]). In reality, there may be additional stable and metastable phases in these binary systems; however, our computational search is limited the supercell sizes we use, initial structures and the limitations structure relaxation in the absence of temperature and pressure for locating global minima. Determining the Gibbs energy of new phases experimentally would require technically intensive heat measurements. Therefore, it would be useful to be able to predict the formation energy of new compounds, using the properties of known compounds. This approaches requires the existence of a parameter around which the structures convergence with a given distribution. Therefore, we choose the quotient of the Gibbs free energy of mixing with respect to the mixing volume, namely

$$\psi(X_i) = \frac{\Delta G_f(X_i)}{\Delta V_f(X_i)} \quad (17)$$

for each known phase i . This parameter can be understood as a mixing pressure which keeps the binary mixture energetically stable and volumetrically consistent against the unary reference systems. The average value for the whole binary system consisting of N known phases is

$$\psi_{\text{mean}} = \frac{1}{N} \sum_{i=1}^N \psi(X_i) \quad (18)$$

and has a standard deviation of

$$\psi_{\text{std}} = \sqrt{\frac{1}{N-1} \sum_{i=1}^N (\psi(X_i) - \psi_{\text{mean}})^2}. \quad (19)$$

Based on the results for $\text{Li}_x\text{Si}_{1-x}$ and $\text{Li}_y\text{C}_{1-y}$ phases represented in Fig. S1, (ESI[†]) the average mixing pressure ψ_{mean} is 7.756 GPa for the Li–Si system and is 3.539 GPa for the Li–C system. The latter data set has a higher standard deviation, which can be attributed to the high anisotropy of the graphitic phases and to the uneven distribution of lithium ions in some phases (e.g. LiC_{24}). However, no conclusions can be reached about the mixing pressure because the computed standard deviations ψ_{std} are solely based on the known phases used as samples, and the variance, ψ_{tol}^2 , from the expected value, ψ_{mean} , must be valid for the whole system. The simplest procedure would be to consider a random sample of phases, which can be considered independent of one another, since they have different atomistic configurations. Indeed, Fig. S2 (ESI[†]) shows how this approach can be applied to both Li–Si and Li–C. The binary mixing pressure for N known phases can be formulated as

$$\psi(N, Pr) = \psi_{\text{mean}}(N) \pm \psi_{\text{tol}}(N, Pr) \quad (20)$$

within a two-sided confidence interval, with the probability Pr . Hence, the two-sided tolerance for the confidence interval can be described using a t -distribution with $N - 1$ degrees of freedom:

$$\psi_{\text{tol}} = \frac{t(N-1, Pr)}{\sqrt{N}} \psi_{\text{std}}. \quad (21)$$

Thus, the heat of formation of any additional phase, whose mixing volume is known, can be empirically predicted as

$$\Delta G_f(X_j, N, Pr) \equiv \Delta V_f(X_j) \psi(N, Pr). \quad (22)$$

Alternatively, this relation can be applied to predict the volume and density of any phase, whose heat of formation is known. Mixing pressure domains have been calculated for the anodic Li–Si and Li–C systems at various confidence intervals and summarized in Table 1.

For the Li–Si system, the energy prediction error of a new $\text{c-Li}_x\text{Si}_{1-x}$ compound would be $\pm 9\%$ with respect to its mixing volume, with a confidence of 0.99. By reducing the confidence level to 0.80, the error would decrease to 4.4%. As previously mentioned, the anisotropy in $\text{Li}_x\text{C}_{1-x}$ structures causes relatively high errors. For a confidence level of 0.99 the error in the mixing pressure reaches 44.7% whereas at 0.80, a phase can be energetically predicted with an error of only 18.1%, with respect to its mixing volume. Based on the mixing pressure distributions found for the Li–Si and Li–C systems, mixing energies have been derived using eqn (22). The resulting phase diagrams are presented in Fig. S3 (ESI[†]). The accuracy of these results depends on the statistical distribution of the mixing pressures $\psi(X_i)$ for the known phases, i .

Further thermodynamic properties such as the chemical potential, the thermodynamic factor, *etc.* can be treated as products of a physico-empirical term related to the mixing pressure and a geometrical term related to the volume. Therefore, the chemical potential of lithium in a binary mixture $\text{Li}_x[\text{H}]$ can be transformed from the eqn (4) and (22) into

$$\mu(x, N, Pr) = \psi(N, Pr) \frac{\partial(\Delta V_f(x))}{\partial x} + \mu_0. \quad (23)$$

Table 1 Mixing pressure, ψ , which is defined as the ratio of the mixing energy to the mixing volume, for binary Li–Si and Li–C (graphite) systems. The arithmetic mean, ψ_{mean} and predicted statistical deviations, ψ_{tol} for N_p computed phases are expressed as a function of the probability, Pr , associated with a confidence interval for each binary system

Probability Pr for a two-sided confidence interval	Li–Si ($\psi_{\text{mean}} = 7.756$ GPa, $N = 18$)			Li–C ($\psi_{\text{mean}} = 3.539$ GPa, $N = 8$)		
	t	ψ_{tol} (GPa)	$\frac{\psi_{\text{tol}}}{\psi_{\text{mean}}}$	t	ψ_{tol} (GPa)	$\frac{\psi_{\text{tol}}}{\psi_{\text{mean}}}$
0.50	0.689	0.177	0.023	0.711	0.321	0.091
0.75	1.191	0.306	0.039	1.254	0.567	0.160
0.80	1.333	0.342	0.044	1.415	0.639	0.181
0.90	1.740	0.447	0.058	1.895	0.856	0.242
0.95	2.110	0.542	0.070	2.365	1.069	0.302
0.99	2.898	0.744	0.096	3.499	1.581	0.447

This leads to

$$\mu(x, N, Pr) = \psi(N, Pr) \left(\frac{\partial(V_{\text{Li}_x[\text{H}]})}{\partial x} - V_{\text{Li}}^0 \right) + \mu_0. \quad (24)$$

By splitting the lithiated electrode material volume into the delithiated host volume, $V_{[\text{H}]}$, and a coefficient of volume expansion, $\lambda(x)$, upon lithiation as

$$V_{\text{Li}_x[\text{H}]} = (1 + \lambda(x))V_{[\text{H}]}, \text{ with } \lambda(x=0) = 0, \quad (25)$$

eqn (23) becomes

$$\mu(x, N, Pr) = \psi(N, Pr) V_{\text{Li}}^0 \left(\frac{V_{[\text{H}]}^0 \partial \lambda(x)}{V_{\text{Li}}^0 \partial x} - 1 \right) + \mu_0. \quad (26)$$

If the system is assumed to be homogeneous, the equilibrium voltage can be derived directly from the eqn (5) and (26):

$$U(x, N, Pr) = \psi(N, Pr) \frac{V_{\text{Li}}^0}{z_{\text{Li}} \mathcal{F}} \left(1 - \frac{V_{[\text{H}]}^0 \partial \lambda(x)}{V_{\text{Li}}^0 \partial x} \right). \quad (27)$$

eqn (27) links the equilibrium voltage to the slope of the volume expansion of the electrode material with respect to the lithium content. For both silicon and graphite anodes, this approximation is valid under the assumption that the quotient, $\psi(N, Pr)$, of the formation energy with respect to the mixing volume is known. Hence, at thermodynamic equilibrium, the maximum voltage would amount to 0.45 ± 0.4 V and 0.31 ± 0.14 V vs. Li/Li^+ with a probability of 99% for silicon and graphite, respectively. A higher value would suggest that thermodynamic equilibrium has not yet been achieved. Furthermore, since the voltage decreases with increasing lithiation, eqn (27) implies for the coefficient of volume expansion that $\partial \lambda(x)/\partial x \geq 0$. In the case of linear volume expansion, e.g. for two-phase (de)lithiation or the deposition of lithium metal, the equilibrium voltage tends to remain constant. The interdependence between mixing energies and volumes and the resulting correlation between voltage and volume expansion should be

studied for further anode and cathode materials that form binary $\text{Li}_x[\text{H}]_{1-x}$ systems.

The crystal structures associated with the compounds lying on the ground state energy lines of the Li-Si and Li-C phase diagrams are represented in Fig. 2.

The orthorhombic LiC phase shown in Fig. 2 exhibits the highest stability and the lowest mixing volume in the Li-C system. In fact, the relatively high Li-C coordination in LiC yields strong coulombic interactions due to the Bader charges of lithium and carbon amounting to $+0.87$ e and -0.87 e within a volume of 3.55 \AA^3 and 19.94 \AA^3 , respectively. Carbon dimers (C2) in LiC have a bond length of 1.26 \AA , which is close to the computational result (1.24 \AA) reported by Matxain *et al.*⁷⁹ Furthermore, the LiC phase is expected to conduct electrons poorly due to its large band gap of 3.349 eV. On the other hand, the carbonaceous structures remain layered at $y \leq 1/6$ in Li_yC due to the strong covalent C-C bonds (1.42 \AA). Below this threshold, lithium is not able to destroy carbon's sp^2 hybridization and thus absorbs at the hollow sites sandwiched between hexagonal C_6 clusters, where it is stabilized by van der Waals and causes a slight increase in the graphite interlayer distance and of the in-plane C-C bonds length. It can also be observed from Fig. 2 that the crystal structures of the $\text{Li}_x\text{Si}_{1-x}$ phases depend on their degree of lithiation, characterized by the mole ratio x . Structures with compositions approaching either pure silicon or lithium tend to be cubic, whereas intermediate systems, such as Li_5Si_2 , exhibit anisotropic arrangements of atoms. In both silicon and graphite host anodes, lithiation results in volumetric changes that can induce cracking. Based on intrinsic material swelling and shrinking behavior observed during cycling, volumetric compensation *via* grain boundaries or pores is expected to help absorb the chemomechanical loading. Lithiation-induced volumetric changes are calculated from the molar volumes (see Fig. 1(c and d)) and are presented in Fig. 3 for silicon and graphite.

The volume expansion that a host structure undergoes when lithiated is shown in Fig. 3. It follows Vegard's law, an empirical

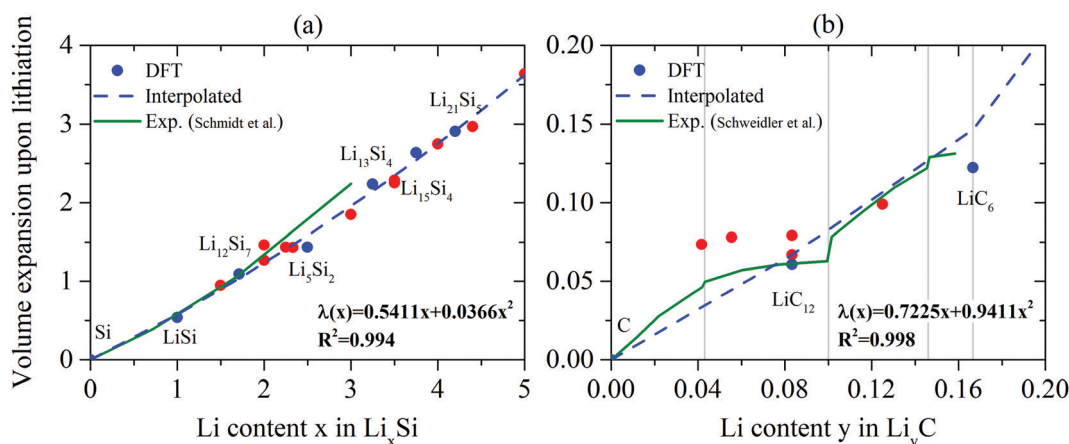


Fig. 3 Volume expansion of (a) silicon and (b) graphite due to lithiation. Stable (blue) and metastable (red) phases are fit to a common second degree polynomial (blue dashed line). The green lines are experimental results at room temperature from Schmidt *et al.*⁸⁰ for amorphous (a-) silicon anodes and from Schweidler *et al.*⁸¹ for carbon anodes. The experimentally observed stages during the lithiation of graphite are separated by gray vertical lines.

observation that geometrical properties vary linearly with the molar concentrations of the species.^{82,83} The volume expansion of from Si to $\text{Li}_{4.2}\text{Si}$ reaches 290%, whereas graphite, with its much lower lithium insertion capacity up to the LiC_6 phase, does not expand by more than 12%. The expansion curves for lithium insertion have slopes of $8.70 \text{ cm}^3 \text{ mol}^{-1}$ (71% of delithiated silicon) for silicon and $3.76 \text{ cm}^3 \text{ mol}^{-1}$ (72% of delithiated graphite) for graphite. Thus, a lithium ion in silicon occupies more than twice the volume of a lithium ion in graphite. As explained previously, the volume expansion which arises from the mixing volume is intrinsically related to the formation energy, *i.e.* to the ability of the electrode host material to absorb additional lithium. Because they allow for unconstrained volumetric expansion, which is required to reach the high capacities silicon offers, porous silicon micro- or nanostructures are very promising. Furthermore, the voids within micro- or nanostructured silicon make them less susceptible to mechanical degradation caused by volume changes, which are the most critical lifetime-limiting mechanisms of silicon anodes. *In situ* measurements of the bulk volume changes of the electrodes throughout cycling are very challenging due to the existence and influence of grain boundaries and pores as well as further electrode components such as conductive carbon, polymer binders and electrolyte components. Nonetheless, available experimental results are in line with our theoretical predictions. By applying potentiostatic measurements to a-Si anodes, Schmidt *et al.*⁸¹ observed that the volume expansion due to lithiation is proportional to the SoC with a proportionality factor close to that predicted from the theoretical results (see Fig. 3(a)). The experimental curve is smoother than the theoretical predictions due to the larger scale of the experimental silicon anode model. Because a- Li_xSi phases are generally less stable than c- Li_xSi phases,²⁵ and therefore have a slightly larger volume, the lithiation-induced volume changes result not only from changes in the lithium content of these phases, but also from their crystallinity. The crystallinity depends on the history of the material including its synthesis, the number of electrochemical cycles as well as the cycling rate. On the other hand, Schweidler *et al.* recently performed rigorous electrochemical characterizations and operando X-ray diffraction (XRD) measurements of the volume expansion of graphite anodes as a function of their lithium content.⁸¹ They observed various coexisting phases causing the voltage plateaus and found a maximum volume expansion of around 13% at LiC_6 (see Fig. 3(b)) which is close to the computational predictions.

From the phase diagrams and molar volumes, theoretical gravimetric and volumetric capacities can be derived using eqn (8). Table S1 (ESI[†]) shows a summary of the capacity of silicon and graphite from this work and from experiments.

In accordance with the Gibbs phase rule, the thermodynamics of Si-C anodes (as two-phase systems) are governed by only two parameters, *e.g.* the lithium content and the interface properties. This means that the silicon to graphitic carbon mole ratio, which determines the mechanical and kinetic response during cycling, does not affect the equilibrium

behavior, since the chemical potential of lithium ions is identical in both silicon and carbon host materials. By neglecting the influence of interfaces on the overall thermodynamic equilibrium, the concentration of lithium ions in each host structure at a given voltage or lithium chemical potential can be predicted directly from the binary bulk phase diagrams. Equilibrium voltage curves determined in this manner are presented in Fig. 4.

the predicted equilibrium voltage for crystalline silicon lies around 0.42 V vs. Li/Li^+ , whereas the voltage derived from the experimental phase diagrams reported by Valencia-Jaime *et al.*²⁸ lies below 0.33 V vs. Li/Li^+ (see Fig. 4(a)). This small differences between DFT and experimental results can be attributed to surfaces and grain boundaries, which would tend to increase the overall lithium chemical potential over against metallic lithium and hence to reduce the voltage. Additionally, finite temperature effects and local amorphization, which would reduce the formation energy drop with respect to the lithium content and thereby decrease the voltage, may contribute to discrepancies between theoretical and experimental results.²⁵ In the case of graphite, its low capacity leads to a limited number of intermediate phases, which nevertheless coexist at thermodynamic equilibrium, leading to the voltage plateaus shown in Fig. 4(b). Despite the small number of Li_yC phases considered in the DFT calculations, the equilibrium voltage curve over the whole lithiation range of graphite is similar to the experimental results determined by Stevens *et al.*³² Overall, the theoretical single-phase voltage predictions from the theoretical volume expansion and mixing pressure for both silicon and graphite anodes agree well with their predicted two-phase voltages; however, these results are most directly applicable to coarse-grained materials, whose bulk structure dominates their macroscopic behavior. Highly nano- and microstructured silicon-carbon-based anodes include a high density of surfaces and interfaces, whose influence also needs to be considered. Indeed, due to this additional degrees of freedom, such materials often fail to exhibit the broad voltage plateaus of bulk-like materials. Thus, capturing the effects of particles' surfaces as well as inter- and intraparticles' interfaces is required to better understand their macroscopic equilibrium behavior.

Li_xSi and Li_yC surfaces as solid-vacuum interfaces

Surface stability or surface tension is expressed in terms of energy per unit area and is typically positive, since spontaneous surface formation would imply that the bulk material is unstable. Surfaces facilitate lithium transport by increasing the contact area with the electrolyte and providing diffusion paths for lithium with low migration energy barriers. We modelled surfaces as solid-vacuum interfaces consisting of single slabs with surface terminations on both sides). Calculations using three different DFT functionals for simulating graphite slabs are shown in Table 2.

The anisotropic structure of graphite favors surface formation parallel to the layers due to the weak interactions between layers. Wang *et al.*⁸⁴ reported an experimental surface

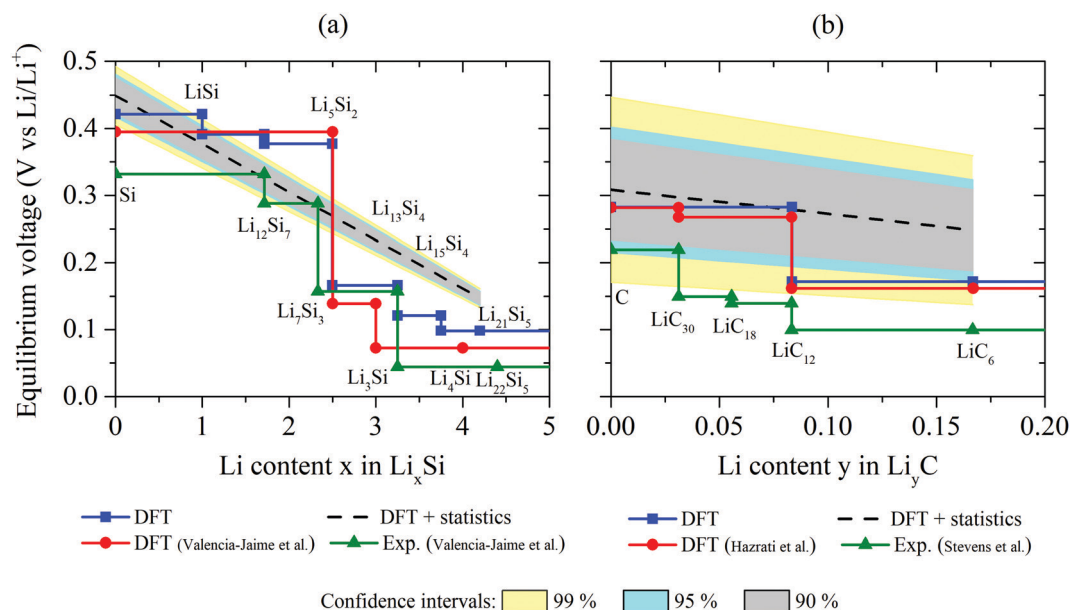


Fig. 4 Equilibrium voltage as a function of the lithium content in (a) c-Si and in (b) graphite host anodes. Equilibrium two-phase voltages are shown as blue solid line with circles. Black dashed lines represent the homogeneous equilibrium voltage assuming a linear correlation between the formation energy and the mixing volume. The yellow, cyan and gray regions represent the predicted voltage, based on the mixing pressure window for each anodic system with a probability of 0.99, 0.95 and 0.90, respectively. Previous DFT simulation results (red loosely dashed line with squares) are taken from the work of Valencia-Jaime *et al.*²⁸ for silicon anodes using GGA-PBE and of Hazrati *et al.*³⁴ for graphite anodes with optB86-vdW. Valencia-Jaime *et al.*²⁸ collected experimental data for the Li-Si system and derived the equilibrium voltages shown as green solid lines in (a). Stevens *et al.*³² investigated lithium insertion in graphite anodes and determined the voltage curve at room temperature, which is shown in (b) as green triangles connect by green solid lines.

tension of 0.39 J m^{-2} for pristine graphite, which is in close agreement with our van-der-Waals corrected theoretical predictions in Table S2 (ESI[†]). Lithium interstitial atoms and adatoms in graphite tend to decrease its surface stability with respect to lithiated bulk graphite and residual metallic lithium and delithiated graphite, suggesting that they might tendentially form metallic, dendritic clusters. In order to further

understand the effects of bulk and surface lithium atoms on the stability of graphite slabs, the charge distributions perpendicular to the surface are plotted in Fig. S7 (ESI[†]). The presence of lithium ions increases the total charge density between the graphite layers while reducing the charge peak at their planar axis. This suggests Coulomb attractions between each lithium ion and the hexagonal C_6 cluster surrounding it,

Table 2 Structure and surface tensions of lithiated graphite surfaces cut parallel to the graphene layers. Carbon is portrayed as black spheres and lithium as blue spheres. The slab thickness and the vacuum gaps are sufficiently large to make interactions between the opposing surfaces negligible

Surface	Adatoms at each slab's side	Slab surface model	Surface tension (J m^{-2})		
			optB86b-vdW	DFT-D2	GGA-PBE
C (0001)	C vs. C		0.230	0.190	-0.001
LiC ₆ (0001)	C vs. C		0.238	0.192	-0.003
LiC ₆ (0001)	C vs. Li		0.565	0.707	0.340
LiC ₆ (0001)	Li vs. Li		0.783	0.871	0.643

which presumably interfere with the van der Waals bonding between adjacent graphite layers. Indeed, lithium bulk and surface atoms exhibit a Bader charge of +0.87 e and +0.69 e, respectively, which implies that even as adatom, lithium likely remains ionic. Moreover, the computed Bader charge for the C₆ cluster is around -0.86 e in the bulk and -0.78 e at the surface. Therefore, Li-C bonding in LiC₆ can be interpreted in terms of delocalization of the 2s valence orbital of lithium within the C₆ cluster without significantly influencing the sp² hybridization of carbon. The fact that lithium adatoms are ionic and that their charge density is similar to that of bulk lithium atoms suggests that bulk and surface lithium atoms will have similar adsorption and migration energies.

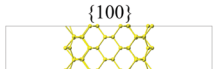
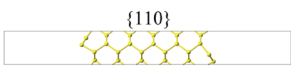
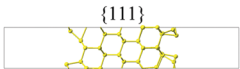
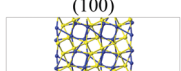
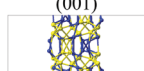
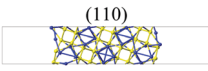
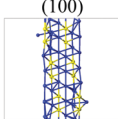
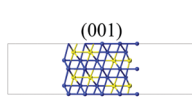
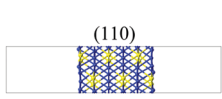
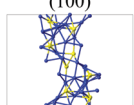
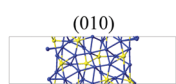
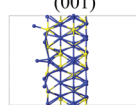
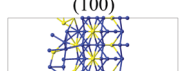
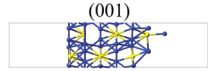
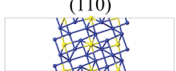
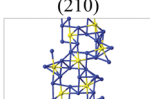
Li_xSi slabs ($x = 0; 1; 2.5; 3.25$ and 4) were also constructed from stable crystals from the phase diagram (see Fig. 1). Li₄Si is used as the representative phase for high lithium content since surfaces built from Li₂₁Si₅, which is slightly more stable, would drastically increase the computation time. Because of the complexity of the Li_xSi structures, significant surface relaxation is often required to reach the lowest energy surface structure for a given orientation. To help the Li_xSi slabs fully relax, AIMD simulations were carried out for 400 fs at 500 K before optimizing the coordinates of the surface atoms. The resulting slabs with their various degrees of lithiation are summarized in Table 3.

The consideration of surface orientations in the main directions of the crystals allows us to understand their anisotropic behavior. Since lithiated Li_xSi phases contain a relatively large number of atoms, the resulting slabs are very large and must be limited in their thickness so that simulations are computationally

reasonable. The slab density (number of atoms per slab area unit) provides a metric for evaluating the slab thickness. We find that the surface tensions of slabs with a slab density higher than 0.2 \AA^{-2} are well converged with respect to slab thickness (see Fig. S4, ESI†). The surface tensions of the Si slabs shown in Table 3 convergence to a value of about 0.02 J m^{-2} . The lithiated Li_xSi slabs in Fig. S5 (ESI†) are presumed to be converged since their slab densities exceed 0.2 \AA^{-2} . Additionally, the total charge density curves in Fig. S8 (ESI†) show a clear difference between the inner and surface atoms, lending additional support to the assumption that the slabs are thick enough to rule out significant interactions between their surfaces. The change in charge densities between the surface atoms and the bulk atoms suggests that the surface only exerts a limited influence on the bulk atoms. The decrease of the total charge density associated with the presence of lithium ions implies that dynamic properties such as phonons and diffusion become less prominent on the potential energy landscape as the lithium concentration increases. Indeed, the elastic stiffness of Li_xSi phases generally decreases upon lithiation.^{28,85} Furthermore, the formation of surfaces disrupts the crystallinity of Li_xSi phases and accelerates the amorphization of silicon anodes. A summary of the surface terminations of Li_xSi phases is shown in Fig. 5.

During surface annealing, the number of dangling bonds of a silicon atom on the {111} and {100} surfaces is reduced to one (see Fig. S6, ESI†). This surface reconstruction is accompanied by an energy dissipation of around 1 J m^{-2} . For {100}, {110} and {111} silicon surfaces, GGA-PBE yields surface energies of 1.263, 1.569 and 1.589 J m^{-2} compared with optB86b, which determines surface tensions of 1.525, 1.725 and 1.815 J m^{-2} , respectively.

Table 3 Li_xSi slabs ($x = 0; 1; 2.5; 3.25$ and 4) with various surface orientations Relaxation and reconstruction were carried out using AIMD simulations in the NVE ensemble with an initial temperature of 500 K, a time step of 2 fs and a total simulation time of 400 fs

System	Slab surface model		
Si			
LiSi			
Li ₅ Si ₂			
Li ₁₃ Si ₄			
Li ₄ Si			
Li ₄ Si			

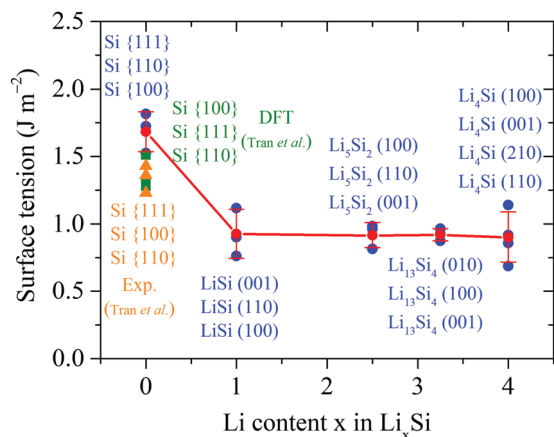


Fig. 5 Surface tensions of lithiated Li_xSi slabs ($x = 0; 1; 2.5; 3.25$ and 4). The red circles and red solid lines represent the statistical averages and standard deviations at each composition. Additional *ab initio* (DFT) values and experimental surface tensions for c-Si are taken from the Materials Project database as summarized in the work of Tran *et al.*³⁶

The differences are mainly due to the additional attractive forces caused by van der Waals interactions considered in the latter method, which results in the breaking of Si-Si bonds to form surfaces requiring more energy. The results using both approaches are about 0.5 J m^{-2} higher than the experimental data reported by Tran *et al.*³⁶ Besides differences between theoretical and real structures, the absence of temperature and pressure may be a reason for the differences. As explained previously, the lower charge density in lithiated Li_xSi surfaces (see Fig. S8, ESI[†]) explains their lower tension, as shown in Fig. 5, compared to pristine silicon surfaces. In contrast to pure silicon, the delocalized bonds in the metallic Li_xSi slabs facilitate the electronic state rearrangement, leading to a lower energy. The same behavior has been observed by Chia-Yun *et al.* in their computational investigation of the lithiation of amorphous $\alpha\text{-Li}_x\text{Si}$ phases.³⁸ The anisotropic atomic arrangement and the different surfaces orientations of c- Li_xSi phases yield variations of their surface tensions about $\pm 0.5 \text{ J m}^{-2}$. When the “average” surface tension, which includes various surface orientations for each Li_xSi phase is considered,

then the surface tension doesn't change significantly as the degree of lithiation is extended beyond $x \geq 1$.

Regardless of their lithium content, Li_xSi surfaces exhibit higher surface tensions than Li_yC surfaces parallel to the graphite layers. As a result, a graphite or graphene coating can be used to protect silicon from electrolytic side-reactions. Due to the finiteness of real anode structures, graphite surfaces with broken C-C bonds and a very high formation energy will also be present (see Table S2, ESI[†]); however, it can be assumed that any carbon atoms with dangling bonds will quickly react with the electrolyte leading to the SEI formation. In the case of Si-C composites, defects in the carbon matrix determine its effectiveness passivating silicon against side reactions and therefore directly determine the overall stability of the anode.

$\text{Li}_x\text{Si-Li}_y\text{C}$ solid-solid interfaces

Based on the equilibrium voltage curves in Fig. 4, solid-solid interfaces would exist as $\text{Li}_x\text{Si-C}$ below a lithium molar concentration of $x = 2.5$ in silicon. The lithiation of graphite up to LiC_6 occurs only after lithium reaches a concentration of 3.25 in silicon. Hence, further lithiation of this two-host anodic system results in the chemical composition $\text{Li}_x\text{Si-LiC}_6$, where $x \geq 3.25$. As described in Section 2.2), $\text{Li}_x\text{Si-Li}_y\text{C}$ interfaces, which can be found in core@shell nanostructures, are constructed based on the geometry of the two adjacent slabs. Following AIMD aimed at aiding structural relaxation, a full geometry optimization including the cell parameters and all atomic coordinates was carried out, as described in Section 2). Pristine graphite and lithiated graphite slabs without lithium adatoms (see Table 2, ESI[†]) are used to build the interfaces with Li_xSi slabs as shown in Fig. 6.

The optimized structures shown in Fig. 6 are three-dimensionally periodic so that the interfaces are repeated. As previously discussed, the thickness of each slab sufficiently minimizes the interactions between the two surfaces of one slab and thus allows us to exclude periodic self-interactions in the interface models. This assumption is further supported by the total charge density in the direction perpendicular to the

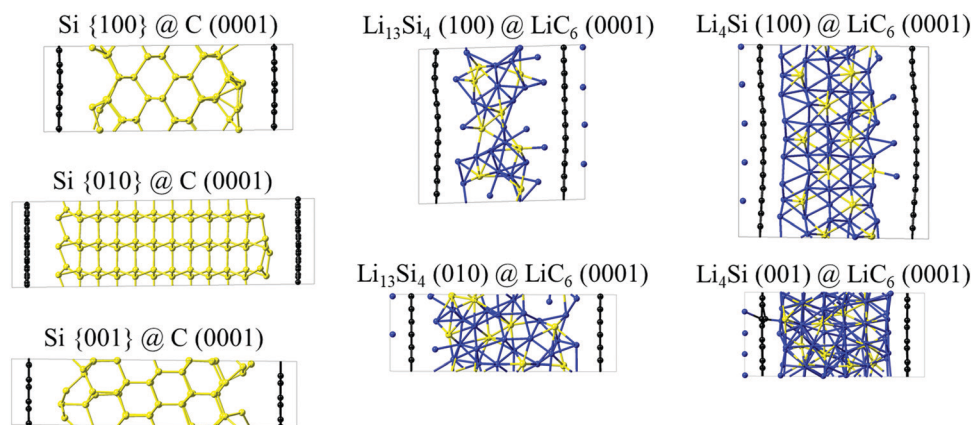


Fig. 6 Heterogeneous (two-phase) $\text{Li}_x\text{Si-Li}_y\text{C}$ systems ($x = 0; 3.25$ and 4 . $y = 0$ and $1/6$) including variously orientated interfaces. The models on the left consist of delithiated Si-C systems whereas the other structures are constructed from Li_xSi and Li_yC slabs. Each cell contains two interfaces.

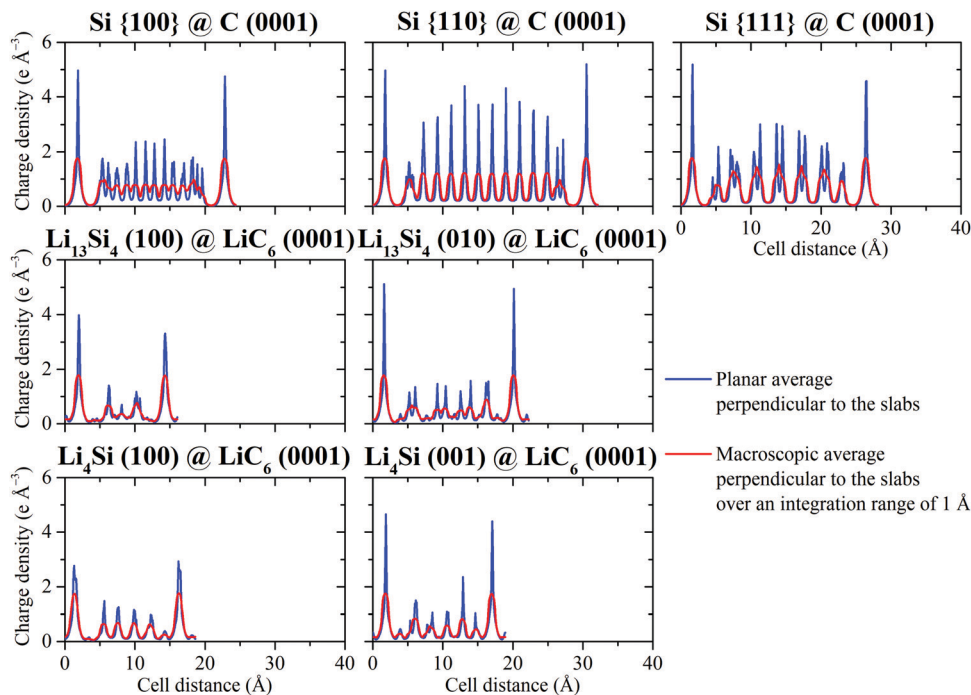


Fig. 7 One-dimensional total-charge-density plots for two-phase $\text{Li}_x\text{Si-Li}_y\text{C}$ interfaces. The blue lines represent the total charge density averaged over planes parallel to the slab whereas the slightly smoothed red lines are the integrated total charge densities for 1 Å regions perpendicular to the slab.

interfaces (see Fig. 7). The electron densities in the graphite layers are slightly lower than those observed within the Li_xSi slabs (see Fig. S7, ESI†), suggesting that the Li_xSi slab is more electronegative than graphite. Nevertheless, when the charge density is interpolated over 1 Å, the influence of Li_xSi on the charge density in the graphite layers almost disappears, offering further support for the sufficiency of two graphite layers to model the bulk, surface and interfacial material responses. The lithiated graphite layers in the $\text{Li}_4\text{Si}(100)\text{-LiC}_6(0001)$ interface (see Fig. 6) are slightly curved due of the high instability of $\text{Li}_4\text{Si}(100)$ slabs (see Fig. 5). This can be seen in the lowering of the charge density peaks at the carbon layers (see Fig. 7).

By comparing the interpolated charge-density curves from the $\text{Li}_x\text{Si-Li}_y\text{C}$ interfaces (Fig. 7) with the charge density of stand-alone Li_xSi (see Fig. S8, ESI†) and Li_yC (see Fig. S7, ESI†) slabs, we observed that solid–solid interfacial adhesion hardly affects the charge density distribution of each phase. Furthermore, the charge density at the solid–solid interfaces is only slightly higher than at the solid–vacuum interfaces. On the other hand, the interfacial stability with respect to the bulk systems can be determined using the interfacial tension described in Section 2.1). The interfacial tensions for the structures shown in Fig. 6 are presented in Fig. 8.

Fig. 8 shows that $\text{Li}_x\text{Si-Li}_y\text{C}$ interfaces have lower interfacial tensions than the delithiated Si–C interfaces, even though lithium ions reduce the stability of the stand-alone graphite slab (see Table 2). Hence, the interfacial stability is primarily determined by the degree of lithiation of the Li_xSi subsystem. As was the case for the surfaces described in Section 3.2), the formation of the interfaces from bulk systems is endothermic, regardless of the

degree of lithiation. Thus, interfaces are metastable and can only be created during synthesis or electrochemical cycling, if thermal or electrochemical energy acts as a driving force.

The mechanical characteristics of solid–solid interfaces or grain boundaries can be expressed in terms of the local volume strain and the normal and cross-sectional strains. Different crystal symmetries and surface orientations coupled with the finiteness of the two slabs or grains result in residual strains even after the interface has been relaxed (see Section 2.1)). For

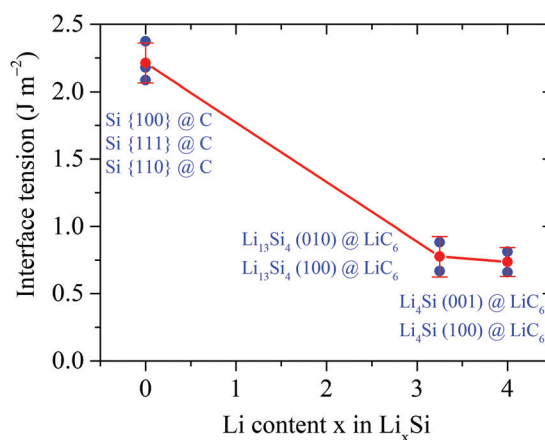


Fig. 8 Interfacial tensions in heterogeneous $\text{Li}_x\text{Si-Li}_y\text{C}$ systems as a function of their lithium content. The red circles connected with solid red lines represent the statistical averages and standard deviations at each concentration.

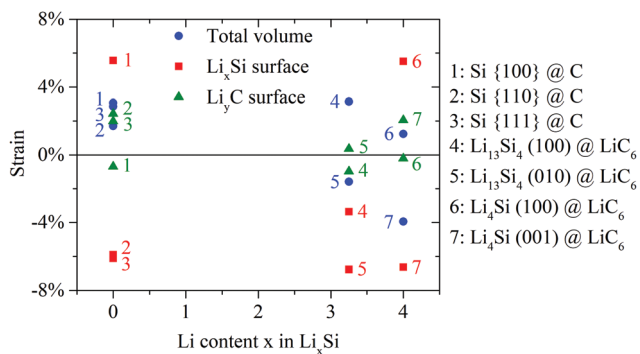


Fig. 9 Residual mechanical volume and surface strains resulting from differences in symmetry and stiffness at the interfaces between Li_xSi and Li_yC phases. The volume strain (blue circles) results from changes in volume resulting from interface formation. The surface strains for Li_xSi (red squares) and Li_yC (green triangles) phases are two-dimensional strains parallel to the interface, which result from interfacial adhesion.

the interfaces shown in Fig. 6, the residual volume strain and the surface strains are presented in Fig. 9.

The presence of both positive and negative values for the volume and surface strains in Fig. 9 reflects the existence of both compression and tension at interfaces, depending on the surface orientations of the grains. The excess width associated with the interface is linearly proportional to the volume strain only in cases, where the surface strain is negligible. A positive volume strain suggests repulsion between the adjacent surfaces. Due to their high mechanical stiffness parallel to their graphene layers, the Li_yC slab experiences less strain than the Li_xSi slabs. In most cases, the Li_xSi slabs experience cross-sectional compression with a negative strain while the Li_yC slabs must responsively undergo tension with positive strain parallel to the interface. However, the reverse behavior is observed for $\text{Si}\{100\}\text{-C}$ and $\text{Li}_4\text{Si}(100)\text{-LiC}_6$ interfaces. A further special case is $\text{Li}_{13}\text{Si}_4(100)\text{-LiC}_6$, where both surfaces undergo a compressive cross-sectional stress and the volume strain is positive. In this case the excess width associated with the interface is significantly larger than in the other systems. On the other hand, a positive volume strain is always found at Si-C surfaces, regardless of the orientation of the silicon surface, which implies repulsion between the delithiated host structures.

Adhesion exists between two surfaces when the energy required to bring them into contact with each other is exothermic (see eqn (13)). In other words, two surfaces adhere when their interfacial tension is lower than the sum of their surface tensions. To better understand the influence of voids on the interfacial stability of $\text{Li}_x\text{Si-Li}_y\text{C}$ two-phase systems, the interfacial tension has been averaged over the various lithium concentrations considered. These average values and their standard deviation are shown in Fig. S9 (ESI[†]). The energy of adhesion at various lithium concentrations was determined from these data points and is plotted in Fig. 10.

Although the presence of voids does not significantly affect the stability of $\text{Li}_x\text{Si-Li}_y\text{C}$ interfaces at the lower SoC bound, *i.e.* at $x = 0$ and $y = 0$, voids can reduce stability at high lithium concentrations by up to 0.5 J m^{-2} . Thus, the increase in stability

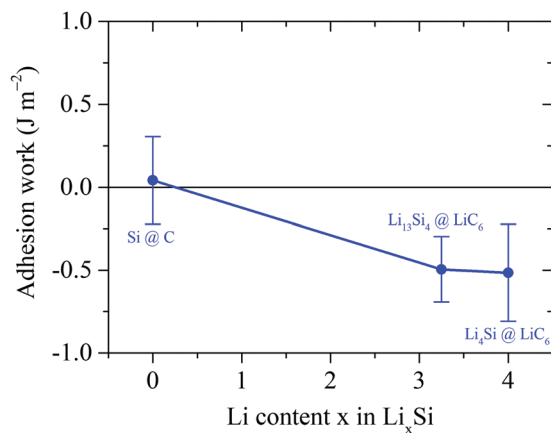


Fig. 10 Average work per unit area for the adhesion of (negative) or repulsion (positive) between Li_xSi and Li_yC phases.

resulting from lithiating $\text{Li}_x\text{Si-Li}_y\text{C}$ is higher than it is for $\text{Li}_x\text{Si-void-Li}_y\text{C}$ interfaces. Consequently, core@shell configurations of Si-C anode nanoparticles prevail at high degrees of lithiation, whereas yolk@shell structures are expected to coexist or even predominate at low lithium concentrations due to adhesion being slightly unfavorable.

Conclusion and outlook

Using first-principles-based electronic-structure calculations, we have computed the key parameters influencing the stability of nanostructured Si-C anodes. We have identified an intrinsic, linear correlation between the mixing enthalpy and mixing volume of both Li-Si and Li-C systems, relating the equilibrium voltage and the volume expansion of these anode materials. Based on the equilibrium voltage curves that we extracted from our computed ground-state phase diagrams for silicon and graphite anodes, we showed that the lithiation of graphite doesn't begin until the lithium content in Li_xSi exceeds $x = 2.5$. We also found that lithium ions stabilize the surfaces and grain boundaries of silicon anodes regardless of their crystallographic orientation and avoid graphite surfaces. Beyond that, the formation of Li_xSi and Li_yC surfaces as well as of $\text{Li}_x\text{Si-Li}_y\text{C}$ interfaces is endothermic, which means that they are only expected to form when thermal treatment or electrochemical cycling provides an appropriate driving force. The strain analysis at the interfaces shows that they generally result in anisotropic mechanical stress fields, which must be taken into account when investigating the mechanical properties of the system. Another important finding is the dependence of the chemical adhesion between the anode host structures on the SoC, especially for nanostructured systems. At low lithium concentrations, graphene-coated silicon nanoparticles thermodynamically prefer a yolk@shell (*i.e.* Si@void@C) configuration. However, lithiation results in a negative energy of adhesion, which favors hollow core@shell (*i.e.* void@Si@C) particles at increasing SoC.

Our results provide insights into the dynamics of silicon-carbon-based nanocomposite anodes by determining the stability of the surfaces and interfaces that define their nanostructures.

Moreover, the synthesis of nanostructures with specific orientations and sizes can only be achieved by properly accounting for the relative stabilities of competing structural motifs. The fact that the presence of lithium ions significantly affects the stability and the adhesion between the anode particles shows that they can lead to the formation of smaller silicon anode particles during synthesis, which might improve the anode material's kinetic and mechanical properties.

Abbreviations

a-	Amorphous
AIMD	<i>Ab initio</i> molecular dynamics
C	Carbon
c-	Crystalline
CG	Conjugate gradient
DFT	Density functional theory
Exp.	Experiment
GGA	Generalized gradient approximation
HF	Hellmann–Feynman
HK	Hohenberg and Kohn
HT	High-throughput
KS	Kohn and Sham
Li	Lithium
PAW	Projector augmented wave
PBE	Perdew, burke and ernzerhof
RMM-DIIS	Residual minimization scheme, direct inversion in the iterative subspace
SCF	Self-consistent-field
SEI	Solid electrolyte interphase or interface
Si	Silicon
SoC	State of charge
STP	Standard temperature and pressure
UNCLE	Universal Cluster expansion
VASP	Vienna <i>ab initio</i> simulation package
vdW	van der Waals

Disclaimer

The results, opinions and conclusions expressed in this publication are not necessarily those of the Volkswagen Group.

Conflicts of interest

There are no conflicts to declare.

Acknowledgements

The research was supported by Volkswagen Group.

References

- B. Zhu, X. Wang, P. Yao, J. Li and J. Zhu, Towards high energy density lithium battery anodes: silicon and lithium, *Chem. Sci.*, 2019, **10**, 7132–7148.
- X. Liu, X. Zhu and D. Pan, Solutions for the problems of silicon-carbon anode materials for lithium-ion batteries, *R. Soc. Open Sci.*, 2018, **5**, 172370.
- M. Ashuri, Q. He and L. L. Shaw, Silicon as a potential anode material for Li-ion batteries: where size, geometry and structure matter, *Nanoscale*, 2016, **8**, 74–103.
- M. Salah, P. Murphy, C. Hall, C. Francis, R. Kerr and M. Fabretto, Pure silicon thin-film anodes for lithium-ion batteries: A review, *J. Power Sources*, 2019, **414**, 48–67.
- X. Zuo, J. Zhu, P. Müller-Buschbaum and Y.-J. Cheng, Silicon based lithium-ion battery anodes: A chronicle perspective review, *Nano Energy*, 2017, **31**, 113–143.
- H. Tian, F. Xin, X. Wang, W. He and W. Han, High capacity group-IV elements (Si, Ge, Sn) based anodes for lithium-ion batteries, *J. Mater.*, 2015, **1**, 153–169.
- B. Liang, Y. Liu and Y. Xu, Silicon-based materials as high capacity anodes for next generation lithium ion batteries, *J. Power Sources*, 2014, **267**, 469–490.
- Z.-L. Xu, X. Liu, Y. Luo, L. Zhou and J.-K. Kim, Nanosilicon anodes for high performance rechargeable batteries, *Prog. Mater. Sci.*, 2017, **90**, 1–44.
- J. Rohrer and K. Albe, Insights into Degradation of Si Anodes from First-Principle Calculations, *J. Phys. Chem. C*, 2013, **117**, 18796–18803.
- K. J. Kim, J. Wortman, S.-Y. Kim and Y. Qi, Atomistic Simulation Derived Insight on the Irreversible Structural Changes of Si Electrode during Fast and Slow Delithiation, *Nano Lett.*, 2017, **17**, 4330–4338.
- J. Asenbauer, T. Eisenmann, M. Kuenzel, A. Kazzazi, Z. Chen and D. Bresser, The success story of graphite as a lithium-ion anode material – fundamentals, remaining challenges, and recent developments including silicon (oxide) composites, *Sustainable Energy Fuels*, 2020, **4**, 5387–5416.
- X. Shen, Z. Tian, R. Fan, L. Shao, D. Zhang, G. Cao, L. Kou and Y. Bai, Research progress on silicon/carbon composite anode materials for lithium-ion battery, *J. Energy Chem.*, 2018, **27**, 1067–1090.
- H. F. Andersen, C. E. L. Foss, J. Voje, R. Tronstad, T. Møkkelbost, P. E. Vullum, A. Ulvestad, M. Kirkengen and J. P. Mæhlen, Silicon-Carbon composite anodes from industrial battery grade silicon, *Sci. Rep.*, 2019, **9**, 14814.
- Y. Cen, R. Sisson, Q. Qin and J. Liang, Current Progress of Si/Graphene Nanocomposites for Lithium-Ion Batteries, *C*, 2018, **4**, 18.
- J. Wang, H. Zhao, J. He, C. Wang and J. Wang, Nano-sized SiOx/C composite anode for lithium ion batteries, *J. Power Sources*, 2011, **196**, 4811–4815.
- X. Lv, W. Wei, B. Huang and Y. Dai, Achieving high energy density for lithium-ion battery anodes by Si/C nanostructure design, *J. Mater. Chem. A*, 2019, **7**, 2165–2171.
- W. Qi, J. G. Shapter, Q. Wu, T. Yin, G. Gao and D. Cui, Nanostructured anode materials for lithium-ion batteries: Principle, recent progress and future perspectives, *J. Mater. Chem. A*, 2017, **5**, 19521–19540.
- B. C. Yeo, H. Jung, H. W. Lee, K.-S. Yun, H. Kim, K.-R. Lee and S. S. Han, Atomistic Simulation Protocol for Improved

- Design of Si–O–C Hybrid Nanostructures as Li-Ion Battery Anodes: ReaxFF Reactive Force Field, *J. Phys. Chem. C*, 2017, **121**, 23268–23275.
- 19 M. Gu, Y. He, J. Zheng and C. Wang, Nanoscale silicon as anode for Li-ion batteries: The fundamentals, promises, and challenges, *Nano Energy*, 2015, **17**, 366–383.
- 20 P. Roy and S. K. Srivastava, Nanostructured anode materials for lithium ion batteries, *J. Mater. Chem. A*, 2015, **3**, 2454–2484.
- 21 S. Goriparti, E. Miele, F. de Angelis, E. Di Fabrizio, R. Proietti Zaccaria and C. Capiglia, Review on recent progress of nanostructured anode materials for Li-ion batteries, *J. Power Sources*, 2014, **257**, 421–443.
- 22 H. Kim, E.-J. Lee and Y.-K. Sun, Recent advances in the Si-based nanocomposite materials as high capacity anode materials for lithium ion batteries, *Mater. Today*, 2014, **17**, 285–297.
- 23 N. Liu, W. Li, M. Pasta and Y. Cui, Nanomaterials for electrochemical energy storage, *Front. Phys.*, 2014, **9**, 323–350.
- 24 H. Wu and Y. Cui, Designing nanostructured Si anodes for high energy lithium ion batteries, *Nano Today*, 2012, **7**, 414–429.
- 25 H. Kim, C.-Y. Chou, J. G. Ekerdt and G. S. Hwang, Structure and Properties of Li–Si Alloys: A First-Principles Study, *J. Phys. Chem. C*, 2010, **115**, 2514–2521.
- 26 M. Jong, W. de; Chen, T. Angsten, A. Jain, R. Notestine, A. Gamst, M. Sluiter, C. Krishna Ande, S. van der Zwaag and J. J. Plata, *et al.*, Charting the complete elastic properties of inorganic crystalline compounds, *Sci. Data*, 2015, **2**, 150009.
- 27 A. Masolin, P.-O. Bouchard, R. Martini and M. Bernacki, Thermo-mechanical and fracture properties in single-crystal silicon, *J. Mater. Sci.*, 2013, **48**, 979–988.
- 28 I. Valencia-Jaime, R. Sarmiento-Pérez, S. Botti, M. A. Marques, M. Amsler, S. Goedecker and A. H. Romero, Novel crystal structures for lithium–silicon alloy predicted by minima hopping method, *J. Alloys Compd.*, 2016, **655**, 147–154.
- 29 N. Li, D. Li, W. Zhang, K. Chang, F. Dang, Y. Du and H. J. Seifert, Development and application of phase diagrams for Li-ion batteries using CALPHAD approach, *Prog. Nat. Sci.: Mater. Int.*, 2019, **29**, 265–276.
- 30 C. Wang, A. J. Appleby and F. E. Litte, Charge–discharge stability of graphite anodes for lithium-ion batteries, *J. Electroanal. Chem.*, 2001, **497**, 33–46.
- 31 V. Pande and V. Viswanathan, Robust high-fidelity DFT study of the lithium-graphite phase diagram, *Phys. Rev. Mater.*, 2018, **2**, 3177.
- 32 D. A. Stevens and J. R. Dahn, The Mechanisms of Lithium and Sodium Insertion in Carbon Materials, *J. Electrochem. Soc.*, 2001, **148**, A803–A811.
- 33 Y. Reynier, R. Yazami and B. Fultz, The entropy and enthalpy of lithium intercalation into graphite, *J. Power Sources*, 2003, **119–121**, 850–855.
- 34 E. Hazrati, G. A. Wijs and G. de; Brocks, Li intercalation in graphite: A van der Waals density-functional study: A van der Waals density-functional study, *Phys. Rev. B: Condens. Matter Mater. Phys.*, 2014, **90**, DOI: [10.1103/PhysRevB.90.155448](https://doi.org/10.1103/PhysRevB.90.155448).
- 35 M. Raju, P. Ganesh, P. R. C. Kent and A. C. T. van Duin, Reactive Force Field Study of Li/C Systems for Electrical Energy Storage, *J. Chem. Theory Comput.*, 2015, **11**, 2156–2166.
- 36 R. Tran, Z. Xu, B. Radhakrishnan, D. Winston, W. Sun, K. A. Persson and S. P. Ong, Surface energies of elemental crystals, *Sci. Data*, 2016, **3**, 160080.
- 37 S. Hara, S. Izumi, T. Kumagai and S. Sakai, Surface energy, stress and structure of well-relaxed amorphous silicon: A combination approach of ab initio and classical molecular dynamics, *Surf. Sci.*, 2005, **585**, 17–24.
- 38 C.-Y. Chou and G. S. Hwang, Surface effects on the structure and lithium behavior in lithiated silicon: A first principles study, *Surf. Sci.*, 2013, **612**, 16–23.
- 39 N. Ooi, A. Rairkar and J. B. Adams, Density functional study of graphite bulk and surface properties, *Carbon*, 2006, **44**, 231–242.
- 40 Z. Zhang, N. Liao, H. Zhou and W. Xue, Insight into silicon-carbon multilayer films as anode materials for lithium-ion batteries: A combined experimental and first principles study, *Acta Mater.*, 2019, **178**, 173–178.
- 41 F. Zhou, N. Liao, M. Zhang and W. Xue, Lithiation behavior of graphene-silicon composite as high performance anode for lithium-ion battery: A first principles study, *Appl. Surf. Sci.*, 2019, **463**, 610–615.
- 42 J. W. Gibbs, *The Collected Works of Nature*, 1929, **124**, 119–120.
- 43 A. Paul, T. Laurila, V. Vuorinen and S. V. Divinski, *Thermodynamics, Diffusion and the Thermodynamics, Diffusion and the Kirkendall Effect in Solids*, Springer, Heidelberg New York, Dordrecht London, 2014.
- 44 M. K. Aydinol, A. F. Kohan, G. Ceder, K. Cho and J. Joannopoulos, *Ab initio* study of lithium intercalation in metal oxides and metal dichalcogenides, *Phys. Rev. B: Condens. Matter Mater. Phys.*, 1997, **56**, 1354–1365.
- 45 M. K. Aydinol and G. Ceder, First-Principles Prediction of Insertion Potentials in Li–Mn Oxides for Secondary Li Batteries, *J. Electrochem. Soc.*, 1997, **144**, 3832.
- 46 K. Persson, Y. Hinuma, Y. S. Meng, A. Van der Ven and G. Ceder, Thermodynamic and kinetic properties of the Li–Graphite system from first-principles calculations, *Phys. Rev. B: Condens. Matter Mater. Phys.*, 2010, **82**, 125416.
- 47 M. K. Aydinol, A. F. Kohan and G. Ceder, *Ab initio* calculation of the intercalation voltage of lithium-transition-metal oxide electrodes for rechargeable batteries, *J. Power Sources*, 1997, **68**, 664–668.
- 48 D. Datta, J. Li, N. Koratker and V. B. Shenoy, Enhanced Lithiation in Defective Graphene, *J. Power Sources*, 2014, **80**, 305–310.
- 49 C. J. Wen and R. A. Huggins, Chemical Diffusion in Intermediate Phases in the Lithium–Silicon System, *J. Solid State Chem.*, 1981, **37**, 271–278.
- 50 Q. Zhang, Y. Cui and E. Wang, First-principles Approaches to Simulate Lithiation in Silicon Electrodes, *Modell. Simul. Mater. Sci. Eng.*, 2013, **21**, 74001.

- 51 I. A. Courtney, J. S. Tse, O. Mao, J. Hafner and J. R. Dahn, Ab initio calculation of the lithium-tin voltage profile, *Phys. Rev. B: Condens. Matter Mater. Phys.*, 1998, **58**, 15583–15588.
- 52 K. T. Butler, G. Sai Gautam and P. Canepa, Designing interfaces in energy materials applications with first-principles calculations, *npj Comput. Mater.*, 2019, **5**, 783.
- 53 S. Wang and H. Ye, Theoretical studies of solid–solid interfaces, *Curr. Opin. Solid State Mater. Sci.*, 2006, **10**, 26–32.
- 54 P. Hohenberg and W. Kohn, Inhomogeneous Electron Gas, *Phys. Rev. [Sect.] B*, 1964, **136**, B864–B871.
- 55 W. Kohn and L. J. Sham, Self-Consistent Equations Including Exchange and Correlation Effects, *Phys. Rev. [Sect.] A*, 1965, **140**, A1133–A1138.
- 56 G. Kresse and J. Furthmüller, Efficiency of ab-initio total energy calculations for metals and semiconductors using a plane-wave basis set, *Comput. Mater. Sci.*, 1996, **6**, 15–50.
- 57 G. Kresse and D. Joubert, From ultrasoft pseudopotentials to the projector augmented-wave method, *Phys. Rev. B: Condens. Matter Mater. Phys.*, 1999, **59**, 1758–1775.
- 58 P. E. Blöchl, Projector augmented-wave method, *Phys. Rev. B: Condens. Matter Mater. Phys.*, 1994, **50**, 17953–17979.
- 59 J. P. Perdew, K. Burke and M. Ernzerhof, Generalized Gradient Approximation Made Simple, *Phys. Rev. Lett.*, 1996, **77**, 3865–3868.
- 60 J. Klimeš, D. R. Bowler and A. Michaelides, van der Waals density functionals applied to solids, *Phys. Rev. B: Condens. Matter Mater. Phys.*, 2011, **83**, DOI: [10.1103/PhysRevB.83.195131](https://doi.org/10.1103/PhysRevB.83.195131).
- 61 J. Klimeš, D. R. Bowler and A. Michaelides, Chemical accuracy for the van der Waals density functional, *J. Phys.: Condens. Matter*, 2010, **22**, DOI: [10.1088/0953-8984/22/2/022201](https://doi.org/10.1088/0953-8984/22/2/022201).
- 62 Z. Wang, S. M. Selbach and T. Grande, van der Waals density functional study of the energetics of alkali metal intercalation in graphite, *RSC Adv.*, 2014, **4**, 3973–3983.
- 63 S. Grimme, Semiempirical GGA-Type Density Functional Constructed with a Long-Range Dispersion Correction, *J. Comput. Chem.*, 2006, **27**, 1787–1799.
- 64 R. P. Feynman, Forces in Molecules, *Phys. Rev.*, 1939, **56**, 340–343.
- 65 H. J. Monkhorst and J. D. Pack, Special points for Brillouin-zone integrations, *Phys. Rev. B: Solid State*, 1976, **13**, 5188–5192.
- 66 A. Jain, S. P. Ong, G. Hautier, W. Chen, W. D. Richards, S. Dacek, S. Cholia, D. Gunter, D. Skinner and G. Ceder, *et al.*, Commentary: The Materials Project: A materials genome approach to accelerating materials innovation: The Materials Project: A materials genome approach to accelerating materials innovation, *APL Mater.*, 2013, **1**, 11002.
- 67 *The AFLOW Library of Crystallographic Prototypes: Part 1*, ed. Mehl, M. J., Hicks, D., Toher, C., Levy, O., Hanson, R. M., Hart, G., Curtarolo, S., 2017, vol. 136.
- 68 D. Lerch, O. Wieckhorst, G. L. Hart, R. W. Forcade and S. Müller, UNCLE: a code for constructing cluster expansions for arbitrary lattices with minimal user-input, *Modell. Simul. Mater. Sci. Eng.*, 2009, **17**, 55003.
- 69 *MedeA version 3.2*; MedeA is a registered trademark of Materials Design, Inc., San Diego, USA.
- 70 J. Sangster, C-Li (Carbon-Lithium) System, *J. Phys. Equil. Diff.*, 2007, **28**, 561–570.
- 71 H. Axel, H. Schäfer and A. Weiss, Zur Kenntnis der Phase Li₂Si₅, *Z. Naturforsch., B: J. Chem. Sci.*, 1966, **21**, 115–117.
- 72 R. Nesper, H. G. von Schnering and J. Curda, Li₁₂Si₇, eine Verbindung mit trigonal-planaren Si₄-Clustern und isometrischen Si₅-Ringern, *Chem. Ber.*, 1986, **119**, 3576–3590.
- 73 U. Frank, W. Müller and H. Schäfer, Zur Kenntnis der Phase Li₁₃Si₄, *Z. Naturforsch., B: J. Chem. Sci.*, 1975, **30**, 10–13.
- 74 M. Gu, Z. Wang, J. G. Connell, D. E. Perea, L. J. Lauhon, F. Gao and C. Wang, Electronic Origin for the Phase Transition from Amorphous Li_xSi to Crystalline Li₁₅Si₄, *ACS Nano*, 2013, **7**, 6303–6309.
- 75 H. Okamoto, The Li-Si (Lithium-Silicon) system, *Bull. Alloy Phase Diagrams*, 1990, **11**, 306–312.
- 76 H. Wu, Z. Xie, Y. Wang, C. Lu and Z. Ma, Modeling diffusion-induced stress on two-phase lithiation in lithium-ion batteries, *J. Mec. Theor. Appl.*, 2018, **71**, 320–325.
- 77 H. Jung, M. Lee, B. C. Yeo, K.-R. Lee and S. S. Han, Atomistic Observation of the Lithiation and Delithiation Behaviors of Silicon Nanowires Using Reactive Molecular Dynamics Simulations, *J. Phys. Chem. C*, 2015, **119**, 3447–3455.
- 78 Y. Lin, T. A. Strobel and R. E. Cohen, Structural Diversity in Lithium Carbides, *Phys. Rev. B: Condens. Matter Mater. Phys.*, 2015, **92**, DOI: [10.1103/PhysRevB.92.214106](https://doi.org/10.1103/PhysRevB.92.214106).
- 79 J. M. Matxain, F. Ruipérez, I. Infante, X. Lopez, J. M. Ugalde, G. Merino and M. Piris, Communication: chemical bonding in carbon dimer isovalent series from the natural orbital functional theory perspective, *J. Chem. Phys.*, 2013, **138**, 151102.
- 80 H. Schmidt, B. Jerliu, E. Hüger and J. Stahn, Volume expansion of amorphous silicon electrodes during potentiostatic lithiation of Li-ion batteries, *Electrochem. Commun.*, 2020, **115**, 106738.
- 81 S. Schweidler, L. de Biasi, A. Schiele, P. Hartmann, T. Brezesinski and J. Janek, Volume Changes of Graphite Anodes Revisited: A Combined Operando X-ray Diffraction and *In Situ* Pressure Analysis Study, *J. Phys. Chem. C*, 2018, **122**, 8829–8835.
- 82 A. R. Denton and N. W. Ashcroft, Vegard's law, *Phys. Rev. A: At., Mol., Opt. Phys.*, 1991, **43**, 3161–3164.
- 83 K. T. Jacob, S. Raj and L. Rannesh, Vegard's law: a fundamental relation or an approximation?, *Int. J. Mater. Res.*, 2013, **98**.
- 84 W. Wang, S. Dai, X. Li, J. Yang, D. J. Srolovitz and Q. Zheng, Measurement of the cleavage energy of graphite, *Nat. Commun.*, 2015, **6**, 7853.
- 85 V. B. Shenoy, P. Johari and Y. Qi, Elastic softening of amorphous and crystalline Li–Si Phases with increasing Li concentration: A first-principles study, *J. Power Sources*, 2010, **195**, 6825–6830.